Article

Fe,Mg-Codoped Bismuth Tantalate Pyrochlores: Crystal Structure, Thermal Stability, Optical and Electrical Properties, XPS, NEXAFS, ESR, and ^{57}Fe Mössbauer Spectroscopy Study

N. A. Zhuk [1,*], M. G. Krzhizhanovskaya [2], A. V. Koroleva [2], V. G. Semenov [2], A. A. Selyutin [2], A. M. Lebedev [3], S. V. Nekipelov [4], D. V. Sivkov [4], V. V. Kharton [5], V. P. Lutoev [6] and B. A. Makeev [6]

[1] Institute of Natural Sciences, Syktyvkar State University, Oktyabrsky Prospect, 55, 167001 Syktyvkar, Russia
[2] Institute of Earth Sciences, Saint Petersburg State University, University Emb. 7/9, 199034 St. Petersburg, Russia
[3] National Research Center-Kurchatov Institute, 1 Akad. Kurchatova Sq., 123182 Moscow, Russia
[4] Institute of Physics and Mathematics of the Komi Science Center UB RAS, Oplesnina st. 4, 167982 Syktyvkar, Russia
[5] Osipyan Institute of Solid State Physics RAS, 142432 Chernogolovka, Russia
[6] Institute of Geology of the Komi Science Center UB RAS, Pervomaiskaya st. 48, 167982 Syktyvkar, Russia
* Correspondence: nzhuck@mail.ru

Abstract: The effect of Fe and Mg-codoping on the crystal structure, optical and dielectric properties of bismuth tantalate-based pyrochlores has been studied. Samples of $Bi_2Mg_xFe_{1-x}Ta_2O_{9.5-\Delta}$ (x ≤ 0.7) are characterized by a porous dendrite-like microstructure. Fe,Mg-codoped bismuth tantalate pyrochlores are thermally stable up to a temperature of 1140 °C (x = 1). The $Bi_2Mg_{0.5}Fe_{0.5}Ta_2O_{9.5-\Delta}$ thermal expansion coefficient increases uniformly and weakly from 3.6 to 9.3 × 10^{-6} °C^{-1} (30–1050 °C). The unit cell parameter of solid solutions increases uniformly from 10.5009(1) Å (x = 0.3) up to 10.5225(7) Å (x = 0.7). The structural parameters of disordered pyrochlore are determined by the Rietveld method (sp. gr. $Fd\bar{3}m$:2 (227), Z = 8). According to near edge X-ray absorption fine structure and X-ray photoelectron spectroscopy data, ions in solid solutions are in the charge states Bi (+3), Mg (+2), Fe (+3), Ta (+5-δ). The Mössbauer spectrum is represented by a symmetric doublet with parameters IS = 0.365 ± 0.0020 mm/s, QS = 0.604 ± 0.034 mm/s, related to Fe^{3+} ions in regular axial octahedral positions. The samples exhibit the properties of dielectrics. The permittivity and the tangent of dielectric losses at 20 °C increases with the growth of iron content in the samples in the range of 28.5–30.5 and 0.001 (1 MHz). The width of the band gap of the obtained materials for direct allowed electronic transitions is in the range of 2.16(5)–2.41(5) eV. The studied samples satisfy the condition of efficient conversion of solar energy into an electrical one and are promising as catalysts and light-absorbing elements for solar panels.

Keywords: pyrochlore; Fe and Mg-codoping; XPS; NEXAFS; Mössbauer spectroscopy; dielectric properties

1. Introduction

Compounds with a pyrochlore-type structure have been attracting the close attention of scientists for many years. These compounds are of great interest due to a wide range of practically useful properties. They are known as photocatalysts, dielectrics, ionic and metallic conductors and exhibit ferro- and ferrimagnetism, giant magnetoresistance, superconductivity and spin glass state [1–5]. Oxide pyrochlores are described by the general formula $A_2B_2O_7$ with a combination of tri-and quadri- ($A^{3+}_2B^{+4}_2O_7$) or di- and pentavalent elements ($A^{2+}_2B^{+5}_2O_7$) in cationic sublattices A and B [6,7]. Such a diverse composition of compounds of this structural type is due to the crystal lattice tolerance to substitutions of cations of both sublattices and to defects in the anionic sublattice. The face-centered cubic

structure of pyrochlores consists of two independent and interpenetrating B_2O_6 and A_2O' sublattices. The cationic sublattice B_2O_6 is formed by octahedra connected at the apex of the angle $[BO_6]$. The A_2O' sublattice has an anticrystobalite structure formed by tetrahedra $[O'A_4]$. Relatively small cations (Ti^{4+}, Hf^{4+}, Ta^{5+}, Sb^{5+}, Nb^{5+}) occupy cationic sites B, and large A ions (Ca^{2+}, Bi^{3+}, Pb^{2+}) are located in the octahedron formed by oxygen atoms of the A_2O' and B_2O_6 sublattices [8–11]. The flexibility of the pyrochlore crystal structure to substitutions of cations of both sublattices and to vacancies in the anionic sublattice makes it possible to significantly vary the composition of compounds and obtain hundreds of compounds of this structural type with various functional properties [12–16].

To describe the stability of the resulting compositions, the concept of "pyrochlore stability field" [6] is used, based on the ratio of cationic radii. The range of values rA/rB = 1.46–1.80 for $A^{3+}_2B^{4+}_2O_7$ and 1.40–2.20 for $A^{2+}_2B^{5+}_2O_7$ limits the stability of pyrochlores. For pyrochlore containing bismuth (III) ions in A-sites and tantalum(V) in B-ones, the ionic radii ratio rA/rB gives a large value equal to 1.83, where $r(Bi^{3+})$ = 1.17 Å (c.n. = 8); $r(Ta^{5+})$ = 0.64 Å (c.n. = 6). For this reason, bismuth tantalate with an equimolar amount of bismuth (III) and tantalum(V) ions does not form a pyrochlore structure and crystallizes in the $BiTaO_4$ structural type [17]. The structure of pyrochlore can be stabilized with an equal ratio of Bi (III) and Ta (V) atoms by doping with ions which ionic radius is smaller than for Bi^{3+} (atoms of 3d elements), as it is shown in studies on triple systems Bi_2O_3–Ta$(Nb,Sb)_2O_5$–$MO(M_2O_3)$ [18–23]. In this case, as a rule, the largest part of the dopant atoms is placed in the octahedral position B, making the bismuth sublattice A_2O' unfilled, which increases the pyrochlore stability.

Chromium-, zinc-, iron- and copper-containing compounds were among the first pyrochlores obtained on the basis of bismuth tantalum [24–28]. A distinctive feature of such pyrochlores is the mixed placement of transition metal cations in two nonequivalent cation sublattices A and, to a greater extent, B. This leads to the formation of a bismuth-defective pyrochlore structure. Moreover, in [29,30] it was shown that the deficiency of bismuth atoms in the A_2O' sublattice cannot be more than 1/3 mole percent and closer to 1/4 due to the stereoactive $6s^2$ electron pair of bismuth atoms. The formation of iron-containing pyrochlores does not satisfy the stability parameter and, for example, for the compositions Bi_2FeTaO_7 and $Bi_2FeTa_2O_{9.5}$ it is equal to 1.82, provided that Fe (III) ions are placed in octahedral positions. In the case when some of the iron (III) ions are placed in the bismuth position, the value of the stability parameter will be within the required interval. The paper [25] shows the possibility of the formation of iron-containing pyrochlores of the general composition $Bi_{3.36}Fe_{2.08+x}Ta_{2.56-x}O_{14.56-x}$ ($-0.32 \leq x \leq 0.48$). Using the data of magnetic susceptibility, and Mössbauer and electron energy loss spectroscopy (EELS) analysis of iron-containing pyrochlores, it was found that iron ions are in the high spin state Fe (III), occupying mainly octahedral positions Nb/Ta/Sb Nb/Ta/Sb [22,23,25,29,31–33]. It was also found that some of the Fe (III) ions can be placed in the bismuth positions. In particular, depending on the composition of ceramics, only 4–15% of A-sites are occupied by Fe^{3+} ions in the pyrochlores of the Bi_2O_3-Fe_2O_3-Nb_2O_5 system [22]. For the Bi_2O_3–Fe_2O_3–Sb_2O_x and $Bi_{1.8}Fe_{0.2}$ (FeSb)O_7 systems the occupation value is equal to 7–25% [23] and 10% [34], respectively. At the same time, it was indicated in [34] that all compositions of $Bi_{2-x}Fe_x$ (FeSb)O_7 (x = 0.1, 0.2, 0.3) demonstrate the state of spin glass due to the presence of some Fe (III) ions in crystallographic positions A. It was found that for pyrochlores in the Bi_2O_3-Fe_2O_3-Nb_2O_5 system, the value of the dielectric constant ε lies in the range of 141–151 and dielectric losses are close to 0.2 at a temperature of 30 °C and frequency of 1 MHz [35]. For pyrochlore $Bi_{1.657}Fe_{1.092}Nb_{1.150}O_7$ the dielectric constant remains high ~120 at 300 K and 1 MHz [22]. Iron-containing pyrochlores $Bi_{3.36}Fe_{2.08+x}Ta_{2.56-x}O_{14.56-x}$ ($-0.32 \leq x \leq 0.48$) are characterized by lower values of the dielectric constant ~78–92 and the dielectric loss tangent ~10^{-1} (MHz, ~30 °C) [25]. Meanwhile, solid solutions $Bi_{3.36}Fe_{2.08+x}Sb_{2.56-x}O_{14.56-x}$ ($0.00 \leq x \leq 0.64$) have lower permittivity values in the range of 24–35 and dielectric losses of the order of 10^{-1} at room temperature and frequency of 1 MHz [36].

Within the work the possibility of the formation of Mg,Fe codoped bismuth tantalate pyrochlores and the influence of magnesium ions on the structure, thermal behavior, symmetry of the local coordination environment of iron (III) ions and optical properties of compounds were demonstrated.

2. Experimental Section

Solid solutions of $Bi_2Mg_xFe_{1-x}Ta_2O_{9,5\pm\Delta}$ (x = 0, 0.3, 0.5, 0.7) were synthesized by the solid-phase method according to the procedure described in detail in [29]. It should be noted that the synthesis was carried out in stages, at temperatures of 650, 850, 950, 1050 °C for 10 h at each calcination stage. The precursors for the solid-phase reaction were the oxides MgO, Bi_2O_3, Fe_2O_3, Ta_2O_5. The microstructure and local elemental composition of the samples were studied by scanning electron microscopy (SEM) and energy dispersive X-ray spectroscopy (EDS) using electron scanning microscope Tescan VEGA 3LMN, (Tescan, Czech), combined with the energy-dispersive spectrometer INCA Energy 450, (Tescan, Czech). X-ray photoelectron spectroscopy (XPS) analysis was performed by the Thermo Scientific ESCALAB 250Xi X-ray spectrometer, (Thermo Fisher Scientific, USA). An X-ray tube with Al K_α radiation (1486.6 eV) was used as a source of ionizing radiation. To neutralize the charge of the sample, an ion-electronic charge compensation system was used. All peaks are calibrated relative to the intensity of the C1s peak at 284.6 eV. The experimental data were processed using the ESCALAB 250 Xi software. The near edge X-ray absorption fine structure (NEXAFS) spectra were measured with a resolution of about 0.45 eV at the NanoPES beamline [37] of the Kurchatov Synchrotron Radiation Source (NRC Kurchatov Institute) using the total electron yield (TEY) mode.

The crystal structure of Fe,Mg-codoped bismuth tantalate was investigated by the powder high-temperature X-ray diffraction (HTXRD) using an X-ray diffractometer Rigaku Ultima IV (Co K_α radiation, air atmosphere, 40 kV/30 mA, Bragg-Brentano geometry) equipped with plastic scintillator strips detector D/teX Ultra. The correctness of 2θ at room temperature (RT) was checked before every measurement using silicon as external standard; the change in zero shift never exceeded $\pm0.02°$ 2θ. The unit-cell parameters were calculated at every temperature step by the Pawley approach and the crystal structure of Fe,Mg-doped bismuth tantalate was refined at 25 °C by the Rietveld method using the Topas 5.0 software package [38]. According to HTXRD data, the crystal structure for the $Bi_2Mg_{0.5}Fe_{0.5}Ta_2O_{9+\Delta}$ composition was refined. The Thompson–Cox–Hastings pseudo-Voigt function was used to describe the reflex profile. Scattering factors of neutral atoms were applied for all atoms. The ideal structure of pyrochlore (space group $Fd\bar{3}m$) was used as the initial structure model. The filling of the positions was determined in accordance with the composition stoichiometry.

For the electron spin resonance (ESR) spectroscopy of the Fe,Mg-codoped bismuth tantalate polycrystalline samples an X-band spectrometer RadioPAN SE/X 2547 was used. The spectra were recorded using a rectangular resonator (RX102, TE 102 mode) at RT as the first derivative, at the high frequency modulation of 100 MHz with the amplitude of 0.25 mT and the microwave power of 35 mW. The pyrochlore sample (45–70 mg) was put into a thin-walled quartz test tube (internal diameter of 2.5 mm) together with the reference sample (anthracite, singlet line g_0 = 2.003, peak to peak distance ΔB_{PP} = 0.5 mT) in an ampoule. For each sample, the spectrum in the magnetic field range of 0–700 mT and the reference line g_0 = 2.003 in the scan range of 5 mT were separately recorded. The intensity of the reference line served as a measure of the gain of the instrument and, when processing spectra, was used to accurately remove background signals from the test tube and ampoule. The spectra were normalized to the reference line intensity and then to 60 mg of the sample. The ESR spectra were recorded with an X-band radiospectrometer SE/X-2547 (RadioPAN) in the Shared Services Center "Geonauka" at the Institute of Geology FRC Komi SC UB RAS.

In order to study electrical properties, metallic Ag electrodes were applied onto both sides of the ceramic discs and sintered at 650 °C for 1 h. The measurements were carried out

with an E7-28 impedancemeter (frequency range of 25–10^7 Hz) at temperatures from 25 up to 450 °C. The thickness and diameter of the studied disk-shaped sample were 1.7–2.3 mm and 14.2–14.3 mm, respectively.

The ^{57}Fe Mössbauer spectra were obtained using an Mössbauer spectrometer Wissel (Wissel, Germany, Starnberg) at the rates of −11–+11 mm/s at RT. The 6×10^8 Bq ^{57}Co in chrome matrix (Ritverc GmbH, St. Petersburg, Russia) at RT was used. To eliminate the texturing effects in the spectra, the samples were prepared in the form of finely ground powder. The duration of spectrum accumulation was about 270 h. The isomeric shift was determined relative to α-Fe.

3. Results and Discussion

3.1. Thermal Behavior, Morphology and Crystal Structure

According to the X-ray phase analysis data, it was found that samples of the composition $Bi_2Mg_xFe_{1-x}Ta_2O_{9.5-\Delta}$ (x = 0.3, 0.5, 0.7, 1.0) crystallize in cubic syngony. The analysis of reflection loss confirmed that the symmetry of the crystal structure is cubic with the space group $Fd\bar{3}m$. It should be noted that the samples of this series were synthesized twice. On the X-ray diffraction patterns of the first series of samples (Figure S1) an admixture of the bismuth orthotantalate was detected, the amount of which decreased with increasing the iron content. The content of bismuth orthotantalate was assessed from X-ray diffraction patterns. For the $Bi_2Mg_xFe_{1-x}Ta_2O_{9.5-\Delta}$ (x = 0.7) sample with the highest content of bismuth orthotantalate, the amount of impurity is no more than 4.86 mass. percent (Figure S2).

The appearance of an impurity and its dependence on the concentration of iron in the samples may be associated with the tendency of Mg (II) ions to be located in two cationic positions of bismuth (III) and tantalum (V), which weakens with an increase in iron and a decrease in magnesium content. Apparently, magnesium ions, being distributed in the Ta(V) positions and having a smaller charge and a larger ionic radius, are capable of causing distortions in the pyrochlore crystal structure due to oxygen vacancies. In order to reduce the degree of stress of the crystal structure, some of the magnesium ions are placed in positions Bi (III) and to create vacancies in bismuth positions, bismuth orthotantalate is released as an impurity. A similar reaction was observed in the case of cobalt-containing pyrochlore [30]. With a decrease in the content of Mg (II) ions in the samples, the stresses of the octahedral frame become weaker and the need for such a process disappears, which can be seen in the experiment. The repeated synthesis of a series of preparations is performed more efficiently. An intermediate and longer homogenization was performed. As a result, pure preparations of solid solutions that do not contain bismuth orthotantalate were synthesized (Figure 1). Based on this, one can conclude that the absence of impurities is due to careful and repeated homogenization of the preparations. Apparently, homogenization contributed to the reduction in local stresses of the structure caused by heterovalent substitution and uniform distribution of ions in the structure, including oxygen vacancies.

With increasing magnesium concentration, the unit cell parameter increases almost uniformly from 10.5009 $\pm$ 0.0001 Å (x = 0.3) up to 10.5225 $\pm$ 0.0007 (x = 0.7). The concentration dependence is almost linear and obeys Vegard's law quite well (Figure 1) [39]. This fact indicates the formation of a continuous series of solid solutions and the distribution of iron and magnesium ions in the same system of crystallographic positions.
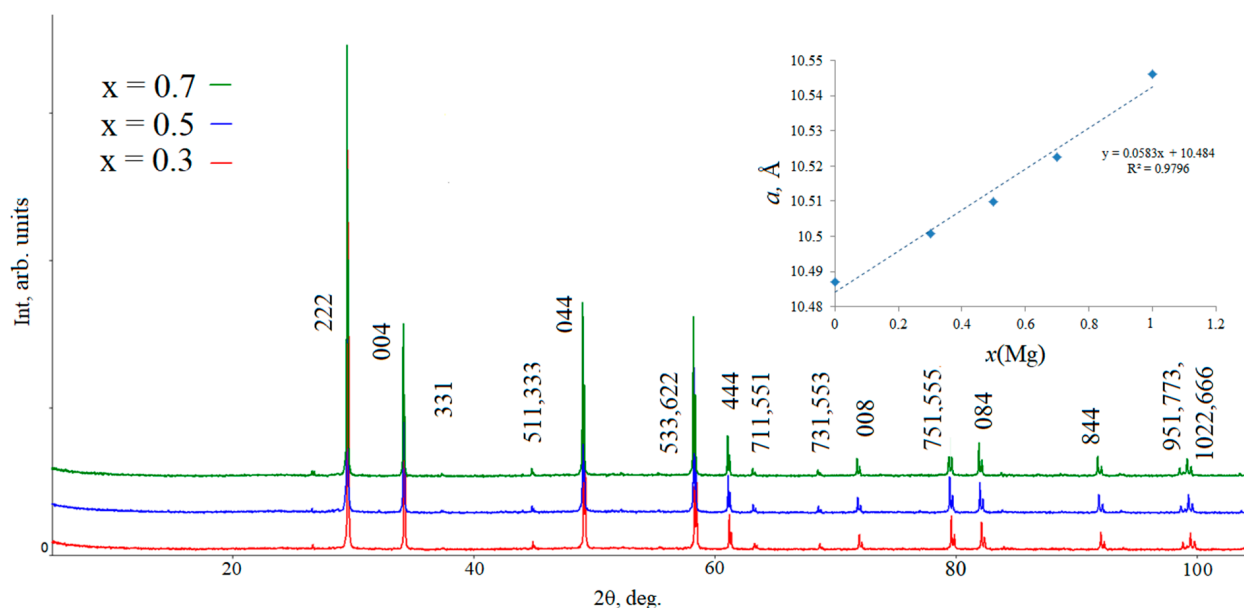
Figure 1. XRD patterns and dependence of the unit cell parameter on the content of magnesium ions of $Bi_2Mg_xFe_{1-x}Ta_2O_{9.5-\Delta}$ (x = 0.3, 0.5, 0.7).

It should be noted that the unit cell parameters previously determined for the extreme terms of the series of the studied solid solution $Bi_{1.5}Mg_{0.75-x}Fe_xTa_{1.5}O_{7\pm\Delta}$ are a = 10.4871(2) Å (x = 0.75) [29] and a = 10.54607 Å (x = 0) [40], which is in good agreement with the parameters of iron- and magnesium-containing solid solutions. The calculated parameters of the solid solution cell are in satisfactory agreement with the cell constant for the border compositions of solid solutions $Bi_2FeTa_2O_{9.5}$ (a = 10.4871 Å) and for $Bi_2MgTa_2O_9$ (a = 10.5461 Å), and are also close to the values given in [25] for iron-containing pyrochlores based on bismuth tantalate $Bi_{3.36}Fe_{2.08+x}Ta_{2.56-x}O_{14.56-x}$ ($-0.32 \leq \times \leq 0.48$) (10.4979–10.5033 Å) and bismuth niobate ($Bi_{1.721}Fe_{0.190}(Fe_{0.866}Nb_{1.134})O_7$) a = 10.508 Å and $Bi_{3.36}Fe_{2.08+x}Nb_{2.56-x}O_{14.56-x}$ ($-0.24 \leq \times \leq 0.48$), for which the parameter varies from 10.5071(4) to 10.5107(7) Å [22,35]. The proximity of the polarization properties and ion radii of Fe (III) and Ta(V) explains the tendency of Fe (III) ions to occupy octahedral positions, repeatedly proven by physicochemical analysis methods [41–43].

Based on powder data, using the software package Topas 5.0, the crystal structure was refined for the compositions $Bi_2Mg_xFe_{1-x}Ta_2O_{9.5-\Delta}$ (x = 0.5, 0.3). The ideal structure of pyrochlore (sp. gr. $Fd\bar{3}m$) served as the initial structure model. The best agreement between the experimental and calculated data was obtained for the disordered structure model, in which the Bi atoms are displaced from the highly symmetrical (16d) positions to the (96g) positions. Tantalum(V) and iron ions are located in the same system of crystallographic positions (16b). The oxygen atoms are disordered and are located in two crystallographic positions, one of which (48f) is completely occupied, the other (8a) is in short supply and filled by 56 (66)%, respectively. For example, the stoichiometric formula of the nominal composition $Bi_2Mg_{0.5}Fe_{0.5}Ta_2O_{9+\Delta}$ (or the normalized formula to 7 oxygen atoms $Bi_{1.4}Mg_{0.35}Fe_{0.35}Ta_{1.4}O_{6.65}$), determined as a result of structure refinement, corresponds to the composition with a deficient sublattice of bismuth cations—$Bi_{1.38}Fe_{0.34}Mg_{0.32}Ta_{1.34}O_{6.69}$. Table 1 shows the results of the refinement of the pyrochlore structure for the compositions $Bi_2Mg_xFe_{1-x}Ta_2O_{9.5-\Delta}$ (x = 0.5, 0.3) by the Rietveld method in the space group $Fd\bar{3}m$:2 (227).

The experimental, calculated, and difference diffraction patterns of $Bi_2Mg_{0.3}Fe_{0.7}Ta_2O_{9.5-\Delta}$ are shown in Figure 2. Atomic and geometric parameters of $Bi_2Mg_xFe_{1-x}Ta_2O_{9.5-\Delta}$ (x = 0.5, 0.3) are presented in Tables 1 and 2, respectively.

Table 1. Parameters of atoms in the $Bi_2Mg_xFe_{1-x}Ta_2O_{9.5-\Delta}$ (x = 0.5; 0.3).

| | | | | x = 0.5 | | | |
Atom	Wyckoff Site	x	y	z	SOF	B_{iso}, Å^2
Bi	96g	0	−0.02489(10)	0.02489(10)	0.1146(7)	1.26(6)
Ta	16b	0.5000	0.5000	0.5000	0.67(6)	0.60(3)
Fe	16b	0.5000	0.5000	0.5000	0.17(6)	0.60(3)
Mg	16b	0.5000	0.5000	0.5000	0.16(6)	0.60(3)
O1	48f	0.1250	0.1250	0.4302(4)	1	1.78(15)
O2	8a	0.1250	0.1250	0.1250	0.56(3)	1.78(15)
				x = 0.3		
Atom	Wyckoff Site	x	y	z	SOF	B_{iso}, Å^2
Bi	96g	0	−0.02516(8)	0.02516(80)	0.1125(4)	0.94(5)
Ta	16b	0.5000	0.5000	0.5000	0.67(6)	0.54(2)
Fe	16b	0.5000	0.5000	0.5000	0.22(6)	0.54(2)
Mg	16b	0.5000	0.5000	0.5000	0.11(6)	0.54(2)
O1	48f	0.1250	0.1250	0.4317(3)	1	1.72(12)
O2	8a	0.1250	0.1250	0.1250	0.66(2)	1.72(12)
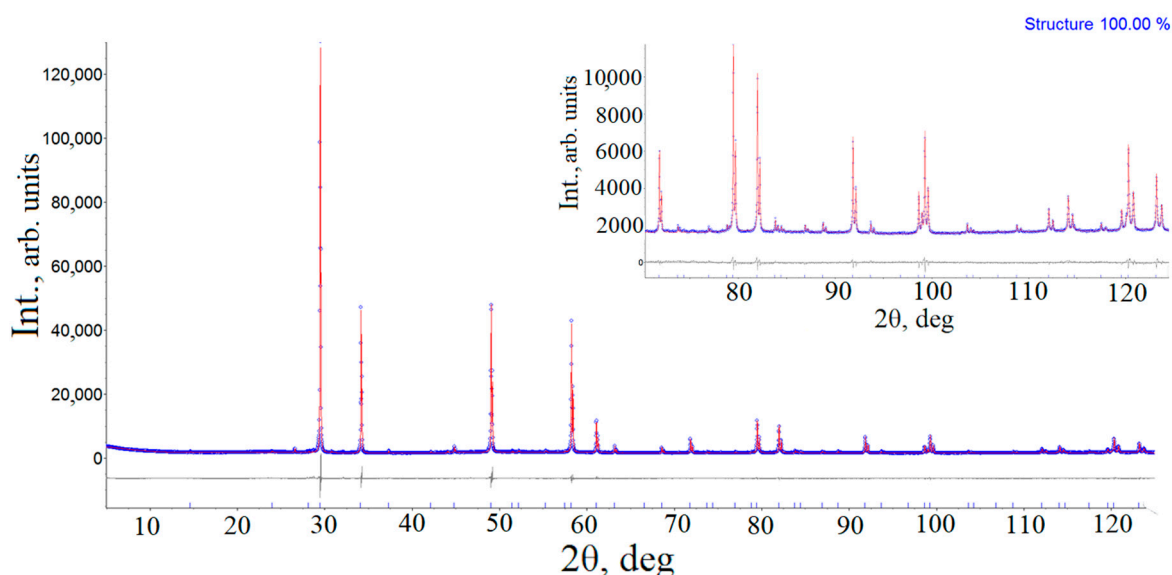
Figure 2. Experimental (blue circles), calculated (solid red line) and difference (gray line) XRD patterns of $Bi_2Mg_{0.3}Fe_{0.7}Ta_2O_{9.5-\Delta}$.

Table 2. Crystallographic data of the $Bi_2Mg_xFe_{1-x}Ta_2O_{9.5-\Delta}$.

Index x	x = 0.5	x = 0.3
a (Å)	10.51036(3)	10.49929(4)
α, β, γ (°)		90, 90, 90
V (Å^3)	1161.053(11)	1157.389(12)
D_{calc} (g/cm^3)	7.57(2)	7.58(1)
R_B	0.63	0.67
R_{wp}	3.16	3.68
R_p	2.26	2.71
R_{exp}	2.16	2.14
GOF	1.46	1.72

According to the simulation results, the tantalum/iron atoms form a regular TaO_6 octahedron with a Ta–O bond length of ~1.9869 Å. Individual interatomic distances in the

weakly ordered BiO_8 polyhedron vary from 2.30 to 2.99 Å (Table 3), with 4 out of 8 bonds noticeably shorter than the others. The asymmetry of the polyhedron of bismuth atoms is due to the distribution of the stereoactive $6 s^2$ pair of bismuth ions.

Table 3. Selected bond lengths in the structure of $Bi_2Mg_xFe_{1-x}Ta_2O_{9.5-\Delta}$.

Index x	x = 0.5	x = 0.3
Bond	**Length (Å)**	**Length (Å)**
Bi1–O1 × 2	2.306(2)	2.304(2)
–O1 × 2	2.344(4)	2.350(3)
–O1 × 2	2.683(3)	2.688(2)
–O2 × 2	2.983(4)	2.987(3)
$<Bi1_{VIII}–O>$	2.58	2.58
Ta1–O1 × 6	1.9959(16)	1.9898(12)
$<Ta1_{VI}–O>$	2.00	1.99

As noted earlier, in the case of pyrochlores based on bismuth tantalate containing atoms of 3d elements [29,30], the formation of a symmetric tantalum–oxygen polyhedron is typical, and the length of the Ta–O bond in the octahedron changes depending on the nature of the 3d atom. In the case of iron ions, the average Ta–O bond length is shorter than, for example, for nickel compositions and the degree of distortion of the BiO_8 polyhedron is lower. Apparently, this is due to the close radii of the Fe (III) and Ta(V) ions [29], distributed in the same system of octahedral sites, and the degree of covalence of the M–O bond (M–Fe (III), Ta(V)).

The samples have a yellow color characteristic of iron (III) compounds, which becomes more intense with increasing iron content (Figure 3).
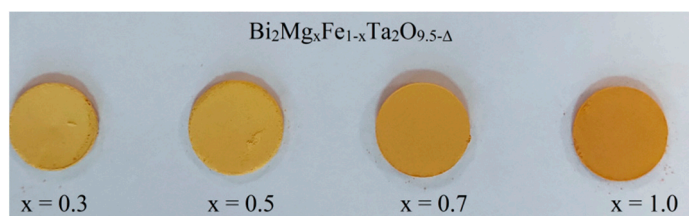

Figure 3. Photographs of the $Bi_2Mg_xFe_{1-x}Ta_2O_{9.5-\Delta}$ (x = 0, 0.3, 0.5, 0.7) ceramics.

The microstructure of the samples is porous, formed by weakly aggregated elongated particles (Figure 4). No significant dependence of the crystallite size on the magnesium/iron ratio has been established. The average size of crystallites determined by the Scherrer method for solid solutions is ∼59.6 nm, meanwhile, larger grains with a longitudinal size of 1–2 μm were recorded by scanning electron microscopy (SEM). In some places, local coalescence of grains with the formation of larger aggregates is observed. It can be noted that an increase in the magnesium content in solid solutions contributes to the appearance of a larger number of grain aggregates. The porosity of the samples according to SEM data varies from 22 (x(Mg) = 0.7) to 28 (x(Mg) = 0.3) percent. Local quantitative analysis by the EDS method showed that the experimental composition of the samples corresponded to the specified one (Figure S3). Elemental mapping of the samples showed a uniform distribution of atoms in the composition of the sample (Figure S4).
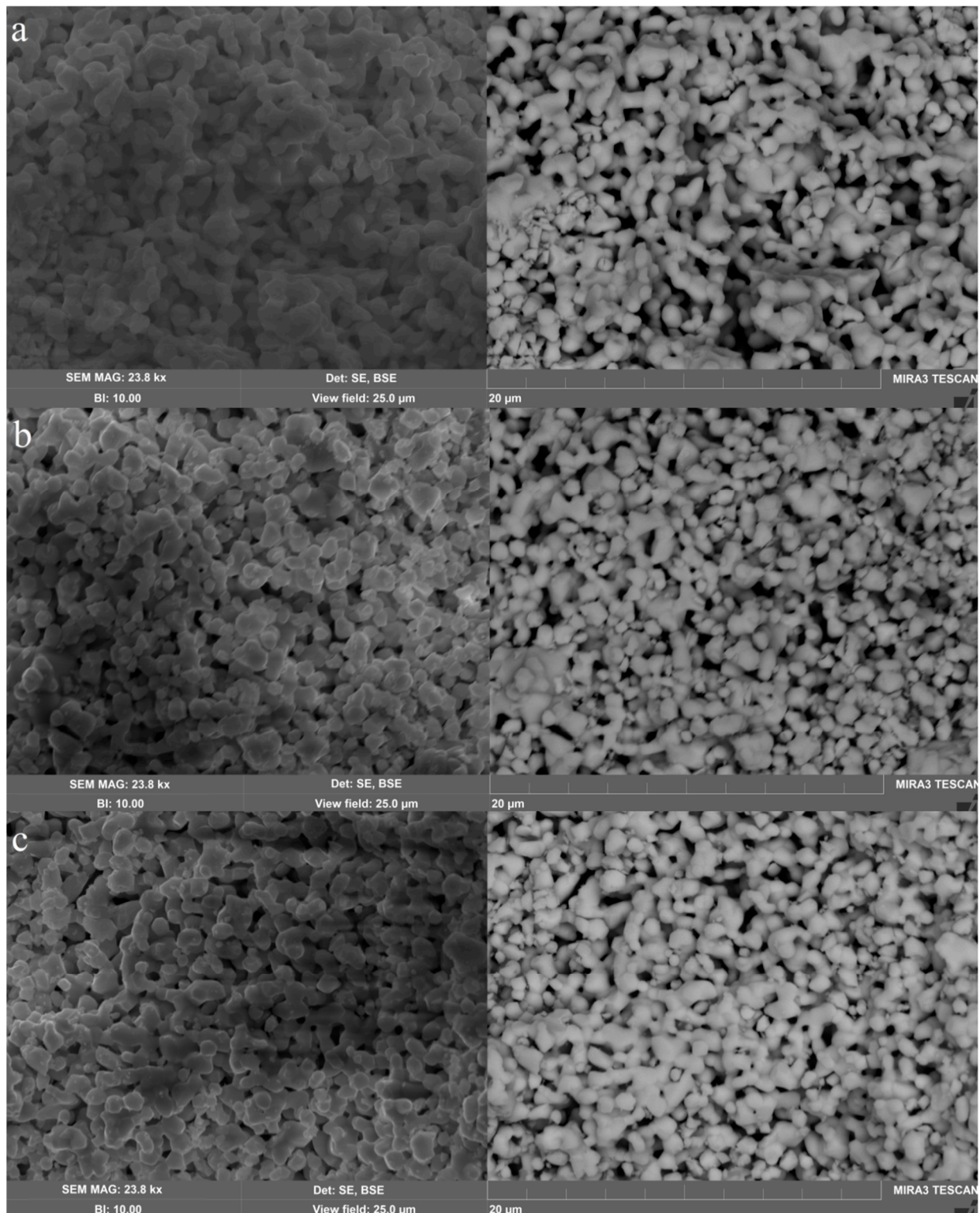
Figure 4. SEM micrographs of the $Bi_2Mg_xFe_{1-x}Ta_2O_{9.5-\Delta}$ ceramics at x = 0.7 (**a**), 0.5 (**b**), 0.3 (**c**).

The study of thermal behavior was carried out by the HTXRD method in the range of 30–1200 °C (Tables S1 and S2). Figure 5a shows the temperature dependence of the cubic unit cell parameter $Bi_2Mg_xFe_{1-x}Ta_2O_{9.5-\Delta}$ (x = 0.5) for the range 30–1200 °C. The unit cell parameter a increases uniformly from 10.50183 Å (30 °C) to 10.57607 Å (1110 °C). A uniform change in the cell constant indicates the absence of phase transformations and the thermal

stability of pyrochlore in the considered temperature range, as was previously revealed for pyrochlores based on bismuth tantalate containing magnesium or 3d ions [29,40,43]. Above 1100 °C, the thermal dissociation of the solid solution probably occurs, as shown for $Bi_2FeTa_2O_{9.5}$ [43]. It is interesting to note that the limiting temperature of the phase stability of $Bi_2Mg_xFe_{1-x}Ta_2O_{9.5-\Delta}$ (x = 0.5) decreases with an increase in the magnesium content from 1140 °C (x = 0) to 1050 °C (x = 1), which may be due to a change the nature of the MO (M-Fe(III), Mg(II) bond in the octahedron from covalent to ionic and the number of oxygen vacancies destabilizing the structure.
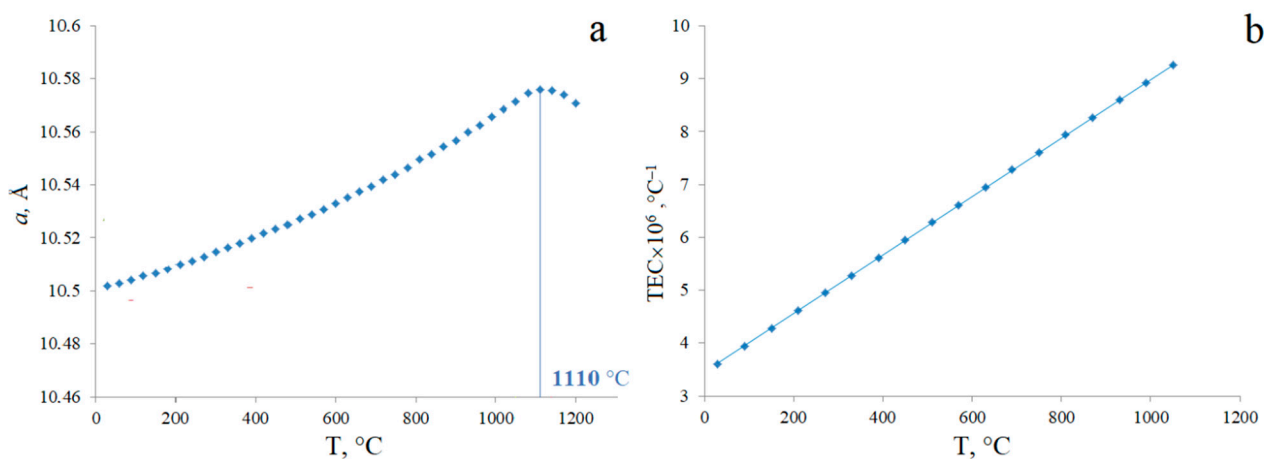
Figure 5. Temperature dependences of unit cell parameter (**a**) and TECs (**b**) of the $Bi_2Mg_{0.5}Fe_{0.5}Ta_2O_{9.5-\Delta}$.

The Figure 5b shows the temperature dependences of the thermal expansion coefficient (TEC) for $Bi_2Mg_{0.5}Fe_{0.5}Ta_2O_{9.5-\Delta}$ calculated as a result of approximation of the temperature dependences of the unit cell parameters.

As can be seen from the Figure 5b, the TEC values for $Bi_2Mg_{0.5}Fe_{0.5}Ta_2O_{9+\Delta}$ increases uniformly and weakly from 3.6 to 9.3×10^{-6} °C^{-1} in the temperature range 30–1050 °C. In this regard, iron–magnesium pyrochlores can be attributed to weakly expanding compounds with isotropic thermal expansion. The average value of TEC (6.4×10^{-6} °C^{-1}) for $Bi_2Mg_{0.5}Fe_{0.5}Ta_2O_{9.5-\Delta}$ in the studied temperature range is comparable to the thermal expansion coefficient of compounds with a framework structure like pyrochlore [44–46], including pyrochlores based on tantalate bismuth containing 3d ions [43]. Taking into account that transition ions are mainly located in octahedral positions, one can speak of a weak effect of the nature of dopants distributed in the three-dimensional cationic sublattice *B* on the thermal expansion of pyrochlores.

3.2. XPS, ESR, NEXAFS and Mössbauer Spectroscopy

The studies of the electronic state of atoms in Mg,Fe-codoped bismuth tantalate pyrochlore were carried out by NEXAFS, XPS, ESR and Mössbauer spectroscopy methods. The chemical state of the surface of the studied samples was investigated by XPS. The obtained XPS spectra of bismuth–magnesium tantalate, Mg,Fe-codoped bismuth tantalate (on the example of a composition with x = 0.5) and corresponding oxides are shown in Figure 6a–d: XPS spectra in a wide energy range of binding energies (20–1400 eV) and spectral dependences in the region of Bi4f-, Bi5d-, Ta4f-, Ta4d-, Mg1s and Fe2p ionization thresholds. The graphs show the results of the decomposition of spectral dependencies into individual peaks, which were modeled by Gauss–Lorentz curves, and the background by Shirley approximation. To study the chemical composition of the samples, only the spectra of metals were analyzed. This is explained by the fact that in the Survey XPS spectrum there is a C1s peak caused by surface contamination of the sample, which can give an indefinite contribution to the intensity of the O1s peak.
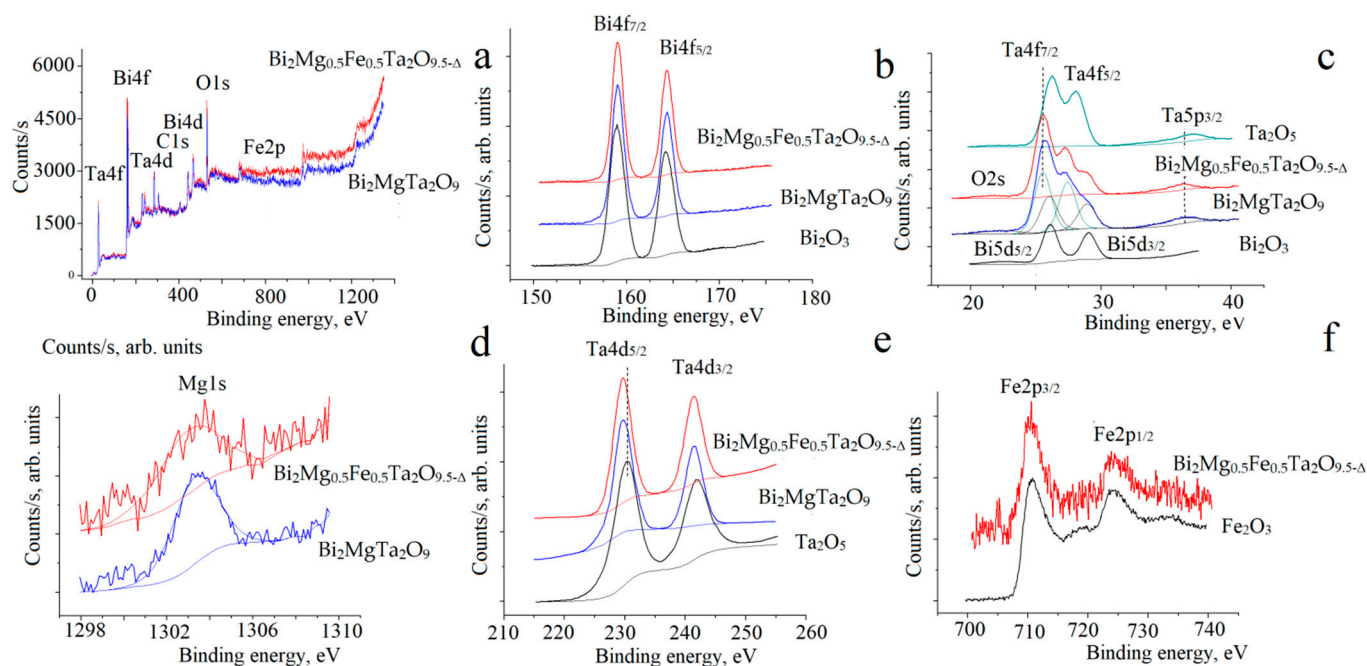
Figure 6. Survey XPS spectra of $Bi_2MgTa_2O_9$ and $Bi_2Mg_{0.5}Fe_{0.5}Ta_2O_{9.5-\Delta}$ (**a**); Bi4f spectra (**b**). For comparison, the spectra of Bi_2O_3 are shown; XPS spectra of tantalum and bismuth atoms (**c**); Mg1s spectra (**d**); Ta4d spectra (**e**); Fe2p spectra of $Bi_2Mg_{0.5}Fe_{0.5}Ta_2O_{9.5-\Delta}$ and of Fe_2O_3 (**f**).

It should be noted that the analyzed spectra in the main details and their energy positions coincide with the previously obtained spectra for the $Bi_2MTa_2O_9$ (M-Co,Ni,Fe), $Bi_2MgTa_2O_9$ pyrochlores [29,30,40,43]. Therefore, it is sufficient to present an analysis of the spectra for one composition at x = 0.5. The energy positions of the $Bi_2MgTa_2O_9$ (1) and $Bi_2Mg_{0.5}Fe_{0.5}Ta_2O_{9+\Delta}$ (2) XPS spectra features are given in Table 4.

Table 4. Energy positions of the components of the XPS spectra of $Bi_2MgTa_2O_9$ (1) and $Bi_2Mg_{0.5}Fe_{0.5}Ta_2O_{9.5-\Delta}$ (2).

Peak	Energy (eV)	
	1	**2**
$Bi4f_{7/2}$	158.99	159.03
$Bi4f_{5/2}$	164.31	164.35
$Bi5d_{5/2}$	25.83	26.11
$Bi5d_{3/2}$	28.85	29.08
$Ta4f_{7/2}$	25.39	25.66
$Ta4f_{5/2}$	27.29	27.56
$Ta4d_{5/2}$	229.57	229.78
$Ta4d_{3/2}$	241.32	241.44
Mg1s	1302.99	1303.19
$Fe2p_{3/2}$	710.47	
$Fe2p_{1/2}$	724.06	
Fe2p sat	718.92	
Fe2p sat	733.10	

Comparison of the observed features with chemical states was carried out on the basis of [47,48]. We note only some features of the newly obtained spectra. First of all, doping with iron ions does not significantly change the spectral characteristics of bismuth, tantalum and magnesium ions (Figure 6a–d). Consequently, the electronic state of these ions remains unchanged and corresponds to the ions Mg (II), Bi (III). In the Ta4f and Ta5p spectra of tantalum atoms, the energy position of the peaks has a characteristic shift towards lower energies compared to the binding energy in pentavalent tantalum oxide Ta_2O_5, which is

characteristic in the case of a decrease in the effective positive charge. The energy shift ΔE in the Ta4f and Ta5p spectra is equal to 0.5 eV, and near the Ta5d edge—to ~1 eV. This suggests that tantalum atoms can have the identical effective charge smaller than five $+(5-\delta)$. Apparently, the observed shift is due to the substitution of tantalum positions with magnesium (II) and iron (III) ions with a lower effective charge. Since any change in the chemical environment of an element affects the spatial redistribution of the charge of its valence electrons, the binding energy of the electrons is consequently changed. The XPS Fe2p spectra of $Bi_2Mg_{0.5}Fe_{0.5}Ta_2O_{9+\Delta}$ (Figure 6d) demonstrate two wide bands $Fe2p_{1/2}$ and $Fe2p_{3/2}$ and their satellites with a characteristic binding energy of 710.47 eV ($Fe2p_{3/2}$), 724.06 eV ($Fe2p_{1/2}$) (Table 4). The coincidence of the $Bi_2Mg_{0.5}Fe_{0.5}Ta_2O_{9+\Delta}$ and Fe_2O_3 oxide spectra by the number and energy positions of the main peaks suggests that iron atoms have an effective charge of +3.

A similar conclusion about the charge state of Fe^{3+} iron atoms in $Bi_2Mg_{0.5}Fe_{0.5}Ta_2O_{9+\Delta}$ follows from the analysis of NEXAFS $Fe2p_{3/2}$ spectra of ceramics and iron oxides shown in Figure 7. In the spectrum there are two broad lines at 707.5 eV and 709 eV, which correlate well with the spectrum of iron in iron (III) oxide in terms of the energy position and shape of the lines. Iron-containing pyrochlore $Bi_2FeTa_2O_{9.5}$ has a similar spectrum shape [29,43].
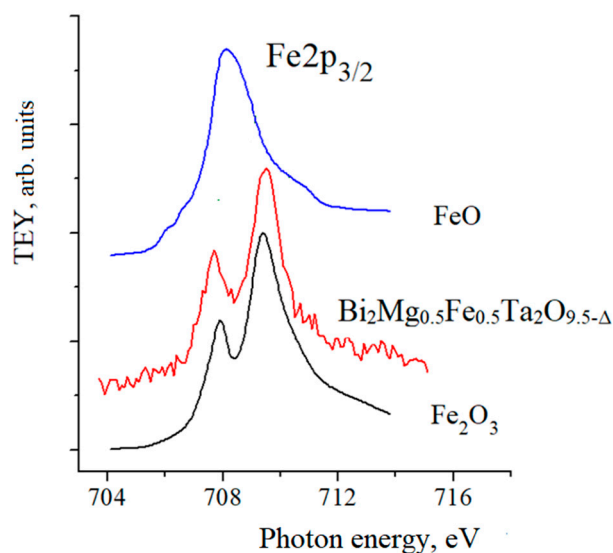

Figure 7. NEXAFS Fe2p spectra of $Bi_2Mg_{0.5}Fe_{0.5}Ta_2O_{9.5-\Delta}$ and iron oxides FeO and Fe_2O_3.

The state of iron (III) ions is confirmed by the data of the ESR spectrum of $Bi_2Fe_{0.5}Mg_{0.5}Ta_2O_{9.5-\Delta}$, in which there is an intense dipole-broadened band from Fe^{3+} ions, split into two components with g ~2.1 and 2.01 with widths of about 80 and 20 mT, respectively. Figure 8 shows for comparison two spectra normalized to one microwave and one gain. They are completely aligned. The spectrum of $Bi_2FeTa_2O_{9.5}$ is naturally wider than the spectrum of iron in $Bi_2Fe_{0.5}Mg_{0.5}Ta_2O_{9.5-\Delta}$ due to the iron content. The vertical line in the figure shows the position of the reference signal with g = 2.003.

The study of the nature of the local environment and the degree of oxidation of iron ions was carried out by the nuclear-gamma-resonance (NGR) method. The Mössbauer spectrum of the $Bi_2Mg_{0.5}Fe_{0.5}Ta_2O_{9+\Delta}$ compound is shown in Figure 9, more precisely the paramagnetic part (-4–$+4$ mm/s) of the full spectrum. About 100% of the area of the spectrum paramagnetic part falls on a symmetrical Fe^{3+} doublet with a chemical shift IS ~0.144 ± 0.009 and a quadrupole splitting QS ~0.600 ± 0.014 mm/s.

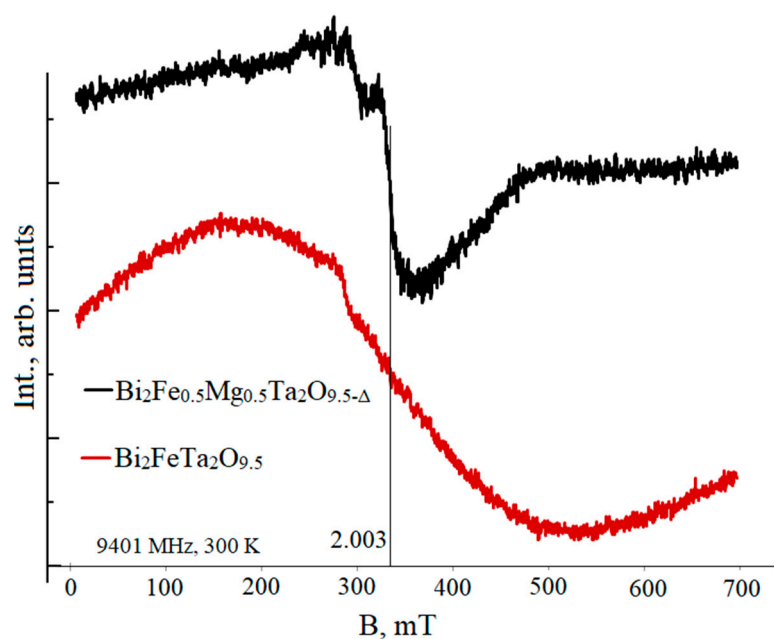**Figure 8.** ESR spectra of the $Bi_2Fe_{0.5}Mg_{0.5}Ta_2O_{9.5-\Delta}$ and $Bi_2FeTa_2O_{9.5}$. Reference sample line with g = 2.003.

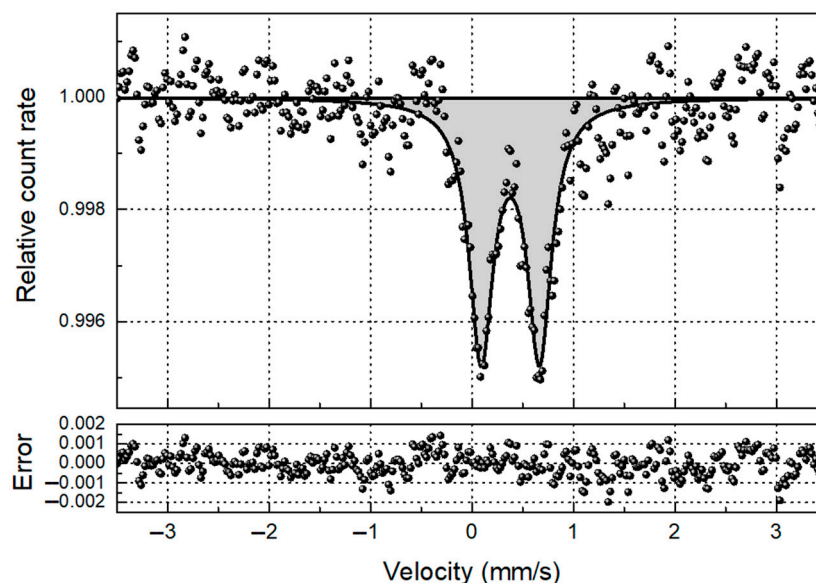**Figure 9.** ^{57}Fe Mössbauer spectra of the $Bi_2Fe_{0.5}Mg_{0.5}Ta_2O_{9.5-\Delta}$ in the paramagnetic region.

According to the data of literature sources and X-ray spectroscopy, the doublet is associated with Fe^{3+} ions in regular axial octahedral positions $Ta^{5+}O_6 + V[O^{2-}] \rightarrow Fe^{3+}O_6$. This assumption does not contradict the results of studies of the NGR spectra of iron-containing compounds in which Fe (III) ions are in octahedral coordination [29,31–34,41]. In particular, for pyrochlore Bi_2FeNbO_7, the parameters of the Mössbaur spectrum of Fe (III) ions occupying octahedral B positions were determined: IS = 0.27 mm/s, QS = 0.66 mm/s [49]. For pyrochlores formed in the Bi–Fe–W–O system, the parameters of the Mössbaur spectrum for octahedral positions are IS = 0.38 mm/s, QS = 0.54 mm/s [31]. The Mössbaur spectrum of pyrochlore $Bi_{1.8}Fe_{0.2}(FeSb)O_7$ exhibits two doublets with parameters IS = 0.38 mm/s, QS = 0.54 mm/s and IS = 0.32 mm/s, QS = 1.87 mm/s, assigned to Fe ions (III) in octahedral positions of antimony (90%) and 8-fold positions of bismuth (10%), respectively [32]. Our NGR data do not contradict the results of X-ray diffraction analysis on the presence of iron

(III) ions in octahedral positions. The assumption that Fe (III) ions replace Bi (III) positions is not supported by the spectrum parameters. Otherwise, an asymmetric signal should appear in the spectrum, described by a doublet with a large quadrupole splitting [31–33], which contradicts our spectrum. It should be noted that the NGR spectrum of iron (III) in $Bi_2Mg_{0.5}Fe_{0.5}Ta_2O_{9.5-\Delta}$ is similar to the spectrum of pyrochlore $Bi_2FeTa_2O_{9.5}$, which does not contain magnesium ions [40]. For them, a signal is observed with practically the same quadrupole splitting QS = 0.575 ± 0.010 and 0.604 ± 0.034 mm/s and close chemical shift IS ~ 0.378 ± 0.005 and 0.365 ± 0.0020 for $Bi_2Mg_{0.5}Fe_{0.5}Ta_2O_{9.5-\Delta}$ and $Bi_2FeTa_2O_{9.5}$, respectively. The shift of the signal to strong fields can be associated with the greatest imperfection of the polyhedral environment of the Fe (III) ions in $Bi_2Mg_{0.5}Fe_{0.5}Ta_2O_{9.5-\Delta}$ due to the heterogeneous replacement of Ta(V) ions by Mg (II) and Fe (III) ions.

Thus, according to near edge X-ray absorption fine structure (NEXAFS) and X-ray photoelectron spectroscopy (XPS) data, Mössbauer spectroscopy study and ESR, iron ions in solid solutions are in the charge state Fe (+3). The Mössbauer spectrum is represented by a symmetric doublet with parameters IS = 0.365(2) mm/s, QS = 0.60(3) mm/s, related to Fe^{3+} ions in regular axial octahedral positions.

3.3. Dielectric and Optical Properties

For samples of solid solutions $Bi_2Mg_xFe_{1-x}Ta_2O_{9.5-\Delta}$ (x = 0.7, 0.5, 0.3) at room temperature, the electrical characteristics were studied—the permittivity and dielectric loss tangent in the frequency range 25 Hz–10 MHz (Figure 10) depending on the ratio magnesium/iron(III).
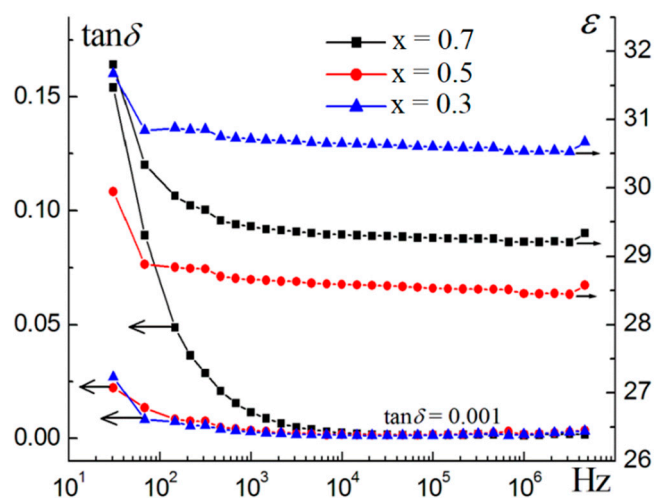

Figure 10. Dependence of the dielectric permeability and the dielectric loss tangent on frequency for the $Bi_2Mg_xFe_{1-x}Ta_2O_{9.5-\Delta}$ at 20 °C.

Measurements of the electrical properties at room temperature (20 °C) showed that the permittivity of the samples is practically independent of frequency and exhibits low values $\varepsilon \approx 28.5–30.5$ ($\upsilon > 10^2$ Hz). In the low-frequency range, the dielectric constant slightly increases by 1–2 units, reaching for x(Mg) = 0.3, values over 32 at 25 Hz. The dielectric loss tangent exhibits a similar course of dependence. Above 10^3 Hz, the loss tangent for all samples does not change and has low values of 0.001 (10^6 Hz). For samples x = 0.5 and 0.7, no noticeable frequency dependence is observed. The exception is the sample with x(Mg) = 0.3, which is characterized by a sharp increase in the dielectric loss tangent at low frequencies. This behavior may be related to the absorption of water by the sample and the tendency of Fe–doped bismuth tantalate pyrochlore [29] to conduct protons. For this reason, the permittivity of a sample with x(Mg) = 0.3 takes on intermediate values of ~29.2 between the values of $\varepsilon \approx 28.5$ (x(Mg) = 0.5) and 30.5 (x(Mg) = 0.7). It should be noted that the permittivity of Fe,Mg-codoped bismuth tantalates is 1.5 times higher than for magnesium-

containing pyrochlores of the same composition [29]. More precisely, for $Bi_2MgTa_2O_9$ at room temperature and a frequency of 1 MHz, the permittivity and dielectric loss tangent are 20 and $2 \cdot 10^{-3}$, respectively. As can be seen from the figure, the dielectric permittivity of the samples depends on the magnesium/iron ratio and takes on the higher values, the more magnesium (II) ions in the samples. This fact conditionally contradicts the concept of the influence of atomic polarizability (α (Mg (II)) = 1.32 $Å^3$, α (Fe (III)) = 2.29 $Å^3$) [25,29]. We have already stated earlier [29] that for polycrystalline materials the influence atomic polarizability on the permittivity secondarily. The grain boundary area has a significant influence on the permittivity. The larger the area, the higher the permittivity. This is achieved by the smaller ceramic grain size. It should be expected that the effect of atomic polarizability will be of paramount importance in the case of single crystals. Studying the microstructure Fe,Mg–codoped bismuth tantalate pyrochlore, we previously noted that an increase in the magnesium content leads to grain intergrowth and a decrease in porosity, a decrease in the area of grain boundaries. This explains why magnesium pyrochlores have an increased dielectric constant. It can be assumed that the dielectric constant, in addition to microstructure, the adsorbed o sample water, as observed for a sample with x(Mg) = 0.3. Apparently, the permittivity increases with increasing sample moisture. The dielectric loss tangent also depends on the ceramic microstructure. The value of the dielectric loss tangent is the lower, the smaller the grain size [29]. In general, the electrical properties of the sample are typical of dielectrics with medium permittivities and low dielectric losses. Having highly porous and fine-grained Fe,Mg–codoped bismuth tantalate pyrochlore ceramics, we investigated its optical properties. Diffuse reflectance spectra of $Bi_2Mg_xFe_{1-x}Ta_2O_{9.5-\Delta}$ (x = 0.7, 0.5, 0.3) solid solution samples are shown in Figure 11.

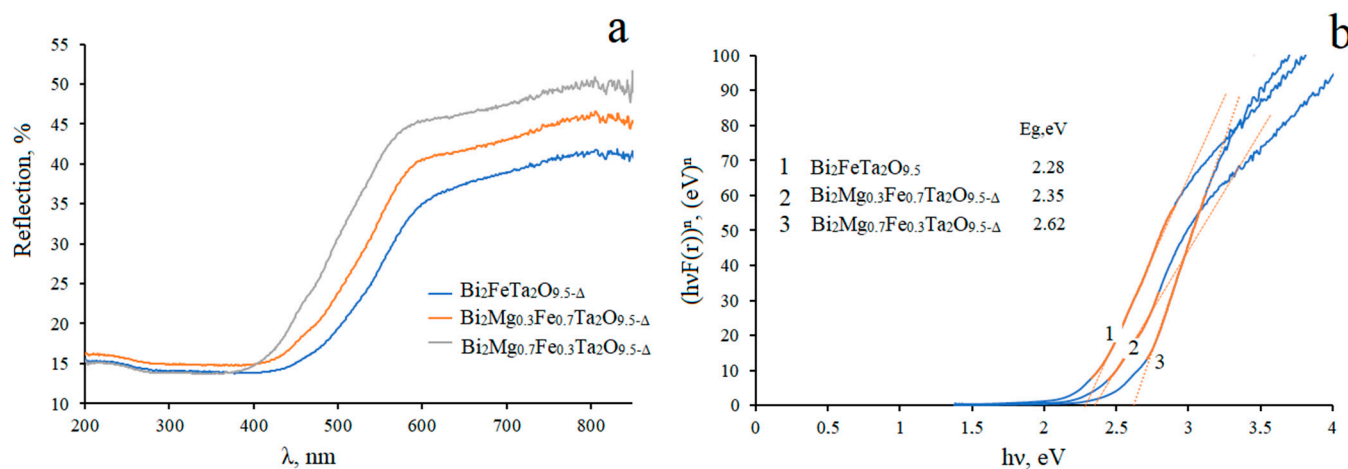**Figure 11.** Diffuse reflectance spectra of the $Bi_2Mg_xFe_{1-x}Ta_2O_{9.5-\Delta}$ samples (**a**), Tauc curves for samples and their corresponding energies of direct allowed transitions (**b**).

The band gap (Eg) of the obtained materials for direct allowed electronic transitions was calculated from the data of the diffuse reflectance spectrum and is in the range of 2.28(5)–2.62(5) eV [49]. All studied samples have a yellow color, the intensity of which increases with an increase in the content of iron (III). This indicates a significant reflection of visible light in the yellow and longer wavelength region of the spectrum. All samples demonstrate a pronounced absorption peak at about 475 nm (~2.63 eV), indicating the presence of iron ions in the trivalent state (Fe^{3+}) with distorted octahedral symmetry [36,37]. Calculations showed that the measured energies of direct allowed electronic transitions, which determine the edge of the absorption band of light quanta, are in the range of 2.28(5)–2.62(5) eV. In this case, with an increase in the iron content in the samples, the band gap decreases, which leads to the convergence of the VZ valence band and the conduction band. A similar effect of doping with iron on the band gap of pyrochlores in the systems Bi_2O_3–Fe_2O_3–TeO_3, Bi-Fe-W-O was noted in [19,31]. The underestimated values of the

band gap in the studied pyrochlores can be a consequence of the Stark effect, as well as the small grain sizes of ceramics. It is interesting to note that the band gap of the studied ceramics correlates with the energy of solar radiation reaching the Earth's surface and having a maximum intensity (2.1–2.5 eV). In this regard, the obtained samples satisfy the condition for efficient conversion of solar energy into electrical energy and are promising as light-absorbing elements for solar batteries.

4. Conclusions

In the work, a continuous series of $Bi_2Mg_xFe_{1-x}Ta_2O_{9.5-\Delta}$ solid solutions synthesized by the solid-phase method was characterized. It has been shown that in the case of insufficient homogenization of preparations during the synthesis, an admixture of bismuth orthotantalate appears. If the thermal stability of the samples is higher, the higher the content of iron ions is. Iron–magnesium pyrochlores are characterized by weak and uniform, isotropic expansion. The average value of TEC in the temperature range of 30–1050 °C is 6.4×10^{-6} °C^{-1}. Solid solutions are characterized by a disordered pyrochlore structure (sp. gr. *Fd$\bar{3}$m:2*, Z = 8), in which iron (III) and tantalum(V) ions share octahedral positions 16b, bismuth ions are displaced to 96g positions. The microstructure of the samples is porous, dendrite-type. According to X-ray spectroscopy, bismuth, tantalum and iron ions are in the charge state Bi (+3), Ta(+5-δ), Fe (+3). The Mössbauer spectrum is represented by a symmetric doublet with IS = 0.378 ± 0.005, QS = 0.575 ± 0.010 mm/s, associated with Fe^{3+} ions in regular axial octahedral positions of tantalum. The samples exhibit typical properties for dielectrics. The band gap of the studied ceramics (2.28(5)–2.62(5) eV) correlates with the energy of solar radiation reaching the Earth's surface and having a maximum intensity.

References

1. Murugesan, S.; Huda, M.N.; Yan, Y.; Al-Jassim, M.M.; Subramanian, V. Band-Engineered Bismuth Titanate Pyrochlores for Visible Light Photocatalysis. *J. Phys. Chem. C* **2010**, *114*, 10598–10605. [CrossRef]
2. Khaw, C.C.; Tan, K.B.; Lee, C.K. High temperature dielectric properties of cubic bismuth zinc tantalate. *Ceram. Intern.* **2009**, *35*, 1473–1480. [CrossRef]
3. Hiroi, Z.; Yamaura, J.-I.; Yonezawa, S.; Harima, H. Chemical trends of superconducting properties in pyrochlore oxides. *Phys. C Supercond. Appl.* **2007**, *460–462*, 20–27. [CrossRef]
4. Bongers, P.F.; van Meurs, E.R. Ferromagnetism in Compounds with Pyrochlore Structure. *J. Appl. Phys.* **1967**, *38*, 944–945. [CrossRef]
5. Greedan, J.E. Frustrated rare earth magnetism: Spin glasses, spin liquids and spin ices in pyrochlore oxides. *J. Alloys Comp.* **2006**, *408–412*, 444–455. [CrossRef]
6. Subramanian, M.A.; Aravamudan, G.; Rao, G.V.S. Oxide pyrochlores—A review. *Prog. Solid State Chem.* **1983**, *15*, 55–143. [CrossRef]
7. McCauley, R.A. Structural Characteristics of Pyrochlore Formation. *J. Appl. Phys.* **1980**, *51*, 290–294. [CrossRef]
8. Pandey, J.; Shrivastava, V.; Nagarajan, R. Metastable $Bi_2Zr_2O_7$ with Pyrochlore-like Structure: Stabilization, Oxygen Ion Conductivity, and Catalytic Properties. *Inorg. Chem.* **2018**, *57*, 13667–13678. [CrossRef]
9. Miles, G.C.; West, A.R. Pyrochlore Phases in the System $ZnO-Bi_2O_3-Sb_2O_5$: I. Stoichiometries and Phase Equilibria. *J. Am. Ceram. Soc.* **2006**, *89*, 1042–1046. [CrossRef]
10. Matteucci, F.; Cruciani, G.; Dondi, M.; Baldi, G.; Barzanti, A. Crystal structural and optical properties of Cr-doped $Y_2Ti_2O_7$ and $Y_2Sn_2O_7$ pyrochlores. *Acta Mater.* **2007**, *55*, 2229–2238. [CrossRef]
11. Srihari, V.; Verma, A.K.; Pandey, K.K.; Vishwanadh, B.; Panchal, V.; Garg, N.; Errandonea, D. Making $Yb_2Hf_2O_7$ Defect Fluorite Uncompressible by Particle Size Reduction. *J. Phys. Chem. C* **2021**, *125*, 27354–27362. [CrossRef]
12. Du, H.; Yao, X. Structural trends and dielectric properties of Bi-based pyrochlores. *J. Mater. Sci. Mater. Electron.* **2004**, *15*, 613–616.
13. Tan, K.B.; Lee, C.K.; Zainal, Z.; Khaw, C.C.; Tan, Y.P.; Shaari, H. Reaction study and phase formation in $Bi_2O_3-ZnO-Nb_2O_5$ ternary system. *Pac. J. Sci. Technol.* **2008**, *9*, 468–479.
14. Hector, A.L.; Wiggin, S.B. Synthesis and structural study of stoichiometric $Bi_2Ti_2O_7$ pyrochlore. *J. Solid State Chem.* **2004**, *177*, 139–145. [CrossRef]
15. Huiling, D.; Xi, Y. Synthesis and dielectric properties development of new thermal stable bismuth pyrochlores. *J. Phys. Chem. Solids.* **2002**, *63*, 2123–2128. [CrossRef]
16. Du, H.; Wang, H.; Yao, X. Observations on structural evolution and dielectric properties of oxygen-deficient pyrochlores. *Ceram. Int.* **2004**, *30*, 1383–1387. [CrossRef]
17. Zhou, D.; Fan, X.Q.; Jin, X.W.; He, D.W.; Chen, G.H. Structures, Phase Transformations, and Dielectric Properties of $BiTaO_4$ Ceramics. *Inorg. Chem.* **2016**, *55*, 11979–11986. [CrossRef]
18. Vanderah, T.A.; Lufaso, M.W.; Adler, A.U.; Levin, I.; Nino, J.C.; Provenzano, V.; Schenck, P.K. Subsolidus phase equilibria and properties in the system $Bi_2O_3:Mn_2O_3\pm x:Nb_2O_5$. *J. Sol. St. Chem.* **2006**, *179*, 3467–3477. [CrossRef]
19. Vanderah, T.A.; Siegrist, T.; Lufaso, M.W.; Yeager, M.C.; Roth, R.S.; Nino, J.C.; Yates, S. Phase Formation and Properties in the System $Bi_2O_3:2CoO_{1+x}:Nb_2O_5$. *Eur. J. Inorgan. Chem.* **2006**, *2006*, 4908–4914. [CrossRef]
20. Valant, M.; Babu, G.S.; Vrcon, M.; Kolodiazhnyi, T.; Axelsson, A.-K. Pyrochlore Range from $Bi_2O_3–Fe_2O_3–TeO_3$ System for LTCC and Photocatalysis and the Crystal Structure of New $Bi_3(Fe_{0.56}Te_{0.44})_3O_{11}$. *J. Am. Ceram. Soc.* **2012**, *95*, 644–650. [CrossRef]
21. Valant, M.; Suvorov, D. The $Bi_2O_3-Nb_2O_5-NiO$ Phase Diagram. *J. Am. Ceram. Soc.* **2005**, *88*, 2540–2543. [CrossRef]
22. Lufaso, M.W.; Vanderah, T.A.; Pazos, I.M.; Levin, I.; Roth, R.S.; Nino, J.C.; Provenzano, V.; Schenck, P.K. Phase formation, crystal chemistry, and properties in the system $Bi_2O_3–Fe_2O_3–Nb_2O_5$. *J. Sol. St. Chem.* **2006**, *179*, 3900–3910. [CrossRef]
23. Egorysheva, A.V.; Ellert, O.G.; Maksimov, Y.V.; Volodin, V.D.; Efimov, N.N.; Novotortsev, V.M. Subsolidus phase equilibria and magnetic characterization of the pyrochlore in the $Bi_2O_3–Fe_2O_3–Sb_2O_x$ system. *J. Alloys Compd.* **2013**, *579*, 311–314. [CrossRef]
24. Chon, M.P.; Tan, K.B.; Zainal, Z.; Taufiq-Yap, Y.H.; Tan, P.Y.; Khaw, C.C.; Chen, S.K. Synthesis and Electrical Properties of Zn-substituted Bismuth Copper Tantalate Pyrochlores. Intern. *J. Appl. Ceram. Tech.* **2016**, *13*, 718–725. [CrossRef]
25. Jusoh, F.A.; Tan, K.B.; Zainal, Z.; Chen, S.K.; Khaw, C.C.; Lee, O.J. Novel pyrochlores in the $Bi_2O_3-Fe_2O_3-Ta_2O_5$ (BFT) ternary system: Synthesis, structural and electrical properties. *J. Mater. Res. Techn.* **2020**, *9*, 11022–11034. [CrossRef]
26. Khaw, C.C.; Tan, K.B.; Lee, C.K.; West, A.R. Phase equilibria and electrical properties of pyrochlore and zirconolite phases in the $Bi_2O_3–ZnO–Ta_2O_5$ system. *J. Eur. Ceram. Soc.* **2012**, *32*, 671–680. [CrossRef]
27. Chon, M.P.; Tan, K.B.; Khaw, C.C.; Zainal, Z.; Taufiq-Yap, Y.H.; Chen, S.K.; Tan, P.Y. Subsolidus phase equilibria and electrical properties of pyrochlores in the $Bi_2O_3–CuO–Ta_2O_5$ ternary system. *J. Alloys Comp.* **2016**, *675*, 116–127. [CrossRef]
28. Kamiyama, T.; Oikawa, K.; Hoshikawa, A.; Kennedy, B.J.; Kubota, Y.; Kato, K. Static bismuth disorder in $Bi_{2-x}(CrTa)O_{7-y}$. *Mater. Res. Bull.* **2004**, *39*, 553–560.
29. Zhuk, N.A.; Sekushin, N.A.; Semenov, V.G.; Fedorova, A.V.; Selyutin, A.A.; Krzhizhanovskaya, M.G.; Lutoev, V.P.; Makeev, B.A.; Kharton, V.V.; Sivkov, D.N.; et al. Dielectric properties, Mössbauer study, ESR spectra of $Bi_2FeTa_2O_{9.5}$ with pyrochlore structure. *J. Alloys Comps.* **2022**, *903*, 163928. [CrossRef]

30. Zhuk, N.A.; Krzhizhanovskaya, M.G.; Koroleva, A.V.; Nekipelov, S.V.; Sivkov, D.V.; Sivkov, V.N.; Lebedev, A.M.; Chumakov, R.G.; Makeev, B.A.; Kharton, V.V.; et al. Spectroscopic characterization of cobalt doped bismuth tantalate pyrochlore. *Sol. St. Sci.* **2022**, *125*, 106820. [CrossRef]

31. Lomakin, M.S.; Proskurina, O.V.; Sergeev, A.A.; Buryanenko, I.V.; Semenov, V.G.; Voznesenskiy, S.S.; Gusarov, V.V. Crystal structure and optical properties of the Bi–Fe–W–O pyrochlore phase synthesized via a hydrothermal method. *J. Alloys Compd.* **2021**, *889*, 161598. [CrossRef]

32. Matsuda, C.K.; Barco, R.; Sharma, P.; Biondo, V.; Paesano, A.; da Cunha, J.B.M.; Hallouche, B. Iron-containing pyrochlores: Structural and magnetic characterization. *Hyperfine Interact.* **2007**, *175*, 55–61. [CrossRef]

33. Filoti, G.; Rosenberg, M.; Kuncser, V.; Seling, B.; Fries, T.; Spies, A.; KemmlerSack, S. Magnetic properties and cation distribution in iron containing pyrochlores. *J. Alloys Comp.* **1998**, *268*, 16–21. [CrossRef]

34. Whitaker, M.J.; Marco, J.F.; Berry, F.J.; Raith, C.; Blackburn, E.; Greaves, C. Structural and magnetic characterisation of the pyrochlores $Bi_{2-x}Fe_x(FeSb)O_7$, (x=0.1, 0.2, 0.3), $Nd_{1.8}Fe_{0.2}(FeSb)O_7$ and $Pr_2(FeSb)O_7$. *J. Solid St. Chem.* **2013**, *198*, 316–322. [CrossRef]

35. Jusoh, F.A.; Tan, K.B.; Zainal, Z.; Chen, S.K.; Khaw, C.C.; Lee, O.J. Investigation of structural and dielectric properties of subsolidus bismuth iron niobate pyrochlores. *J. Asian Ceram. Soc.* **2020**, *8*, 957–969. [CrossRef]

36. Jusoh, F.A.; Tan, K.B.; Zainal, Z.; Chen, S.K.; Khaw, C.C.; Lee, O.J.; Balachandran, R.; Murthy, H.C.A. Novel pyrochlore-structured bismuth iron antimonates: Structural, impedance and electrochemical studies. *Results Phys.* **2021**, *27*, 104542. [CrossRef]

37. Lebedev, A.M.; Menshikov, K.A.; Nazin, V.G.; Stankevich, V.G.; Tsetlin, M.B.; Chumakov, R.G. NanoPES Photoelectron Beamline of the Kurchatov Synchrotron Radiation Source. *J. Surf. Investig. X-ray Synchrotron Neutron Tech.* **2021**, *15*, 1039–1044. [CrossRef]

38. Bruker, A.X.S. *Topas 5.0. General Profile and Structure Analysis Software for Powder Diffraction Data*; Bruker A.X.S.: Karlsruhe, Germany, 2014.

39. Vegard, L. Die Konstitution der Mischkristalle und die Raumfüllung der Atome. *Z. Phys.* **1921**, *5*, 17–26. [CrossRef]

40. Zhuk, N.A.; Krzhizhanovskaya, M.G. Thermal expansion of bismuth magnesium tantalate and niobate pyrochlores. *Ceram. Int.* **2021**, *47*, 30099–30105. [CrossRef]

41. Zhuk, N.A.; Lutoev, V.P.; Lysyuk, A.Y.; Makeev, B.A.; Belyy, V.A.; Nekipelov, S.V.; Sivkov, V.N.; Koroleva, A.V.; Krzhizhanovskaya, M.G.; Beznosikov, D.S. Thermal behavior, magnetic properties, ESR, XPS, Mössbauer and NEXAFS study of Fe-doped $CaCu_3Ti_4O_{12}$ ceramics. *J. Alloys Compd.* **2021**, *855*, 157400. [CrossRef]

42. Zhuk, N.A.; Lutoev, V.P.; Belyy, V.A.; Makeev, B.A.; Beznosikov, D.S.; Nekipelov, S.V.; Yermolina, M.V. EPR and NEXAFS spectroscopy of $BiNb_{1-x}Fe_xO_{4-\delta}$ ceramics. *Phys. B Condensed Matter.* **2019**, *552*, 142–146. [CrossRef]

43. Zhuk, N.A.; Krzhizhanovskaya, M.G.; Koroleva, A.V.; Reveguk, A.A.; Sivkov, D.V.; Nekipelov, S.V. Thermal expansion, crystal structure, XPS and NEXAFS spectra of Fe-doped bismuth tantalate pyrochlore. *Ceram. Intern.* **2022**, *48*, 14849–14855. [CrossRef]

44. Shukla, R.; Vasundhara, K.; Krishna, P.S.R.; Shinde, A.B.; Sali, S.K.; Kulkarni, N.K.; Achary, S.N.; Tyagi, A.K. High temperature structural and thermal expansion behavior of pyrochlore-type praseodymium zirconate. *Intern. J. Hydrogen Energy.* **2015**, *40*, 15672–15678. [CrossRef]

45. Feng, J.; Xiao, B.; Zhou, R.; Pan, W. Thermal expansions of $Ln_2Zr_2O_7$ (Ln = La, Nd, Sm, and Gd) pyrochlore. *J. Appl. Phys.* **2012**, *111*, 103535. [CrossRef]

46. Raison, P.E.; Pavel, C.C.; Jardin, R.; Suard, E.; Haire, R.G.; Popa, K. Thermal expansion behavior of $Ce_2Zr_2O_7$ up to 898 K in conjunction with structural analyses by neutron diffraction. *Phys. Chem. Miner.* **2010**, *37*, 555–559. [CrossRef]

47. Khairallah, F.; Glisenti, A. XPS Study of MgO Nanopowders Obtained by Different Preparation Procedures. *Surf. Sci. Spectra* **2006**, *13*, 58–71. [CrossRef]

48. Regan, T.J.; Ohldag, H.; Stamm, C.; Nolting, F.; Luning, J.; Stöhr, J.; White, R.L. Chemical effects at metal/oxide interfaces studied by x-ray-absorption spectroscopy. *Phys. Rev. B* **2001**, *64*, 214422. [CrossRef]

49. Botella, P.; Errandonea, D.; Garg, A.B.; Rodriguez-Hernandez, P.; Muñoz, A.; Achary, S.N.; Vomiero, A. High-pressure characterization of the optical and electronic properties of $InVO_4$, $InNbO_4$, and $InTaO_4$. SN. *Appl. Sci.* **2019**, *1*, 389.